Profiling oocytes with neural networks from images and mechanical data

Samuel Lamont, Juliette Fropier, Joël Abadie, Emmanuel Piat, Andrei Constantinescu, Franck J Vernerey

Available online at www.sciencedirect.com

ScienceDirect

Journal Logo

00 (2023) 1–27

Profiling Oocytes with Neural Networks from Images and Mechanical Data

Samuel Lamont[a], Juliette Fropier[c], Joel Abadie[b], Emmanuel Piat[b], Andrei Constantinescu[c], Christophe Roux[d], Franck Vernerey[a,*]

[a] *Department of Mechanical Engineering, Program of Materials Science and Engineering, University of Colorado Boulder, Boulder, Colorado 80309*

[b] *FEMTO-ST Institute, Univ. Bourgogne Franche-Comté, CNRS, 15B avenue des Montboucons, 25030 Besançon, cedex, France*

[c] *Laboratoire de Mécanique des Solides - CNRS - École Polytechnique - Institut Polytechnique de Paris, 91128, Palaiseau, France*

[d] *Service de Biologie et Médecine de la Reproduction – Cryobiologie - CECOS Franche-Comté Bourgogne, CHRU Jean Minjoz, 3 Bd Fleming, 25030 Besançon cedex*

Abstract

The success rate of assisted reproductive technologies could be greatly improved by selectively choosing egg cells (oocytes) with the greatest chance of fertilization. The goal of mechanical profiling is, thus, to improve predictive oocyte selection by isolating the mechanical properties of oocytes and correlating them to their reproductive potential. The restrictions on experimental platforms, however – including minimal invasiveness and practicality in laboratory implementation – greatly limits the data that can be acquired from a single oocyte. In this study, we perform indentation studies on human oocytes and characterize the mechanical properties of the zona pellucida, the outer layer of the oocyte. We obtain excellent fitting with our physical model when indenting with a flat surface and clearly illustrate localized shear-thinning behavior of the zona pellucida, which has not been previously reported. We conclude by outlining a promising methodology for isolating the mechanical properties of the cytoplasm using neural networks and optical images taken during indentation.

Keywords:
Inverse Problems, Neural Networks, Mechanical Characterization, Transient Network Theory, Mechanics

1. Introduction

Isolating the mechanical properties of multi-component biological structures presents a uniquely challenging inverse problem that is widespread in the field of bio-characterization [1, 2, 3]. Many times, it is impossible to directly probe the response of individual components, such as the interior and exterior regions of cell, making it difficult to characterize their mechanical properties. Properly characterizing each

*Corresponding author
Email address: franck.vernerey@colorado.edu (Franck Vernerey)

component is highly desirable, however, as their mechanical behavior may highlight biological properties – in the case of the oocyte, fertility. Due to this, we commonly rely on indirectly characterizing the components, which introduces costly and badly posed inverse problems, to backtrack the mechanical parameters. Developing reliable and efficient methods for solving these problems would, thus, be beneficial for many bio-characterization applications including predictive oocyte selection for assisted reproductive technologies (ARTs).

The potential for using mechanical properties as a metric for oocyte fertility has been largely established. One of the most promising properties is the stiffness of the zona pellucida, which has been categorically linked to fertilization [4, 5, 6, 7, 8, 9, 10]. Most of these studies, however, were performed on oocytes both before and after successful fertilization; a standard metric for predicting the fertility of an oocyte based on the stiffness of its zona prior to use in ART has not yet been proposed. Thus, while most sources agree that the stiffness of the zona should be considered, it is likely not a sufficient indicator of fertility by itself. The viscosity of the cytoplasm has also been qualitatively linked to fertility in injection tests [11]. Reliably measuring this quantity has remained difficult experimentally, however, as the cytoplasm does not likely contribute to the mechanical responses that are accessible using an ART-compatible experimental protocol [12]. Due to the difficulty of reliably measuring the mechanical properties of the oocyte, morphological characterization and selection is still widely preferred for ART protocols [13].

The first limitation of oocyte profiling involves collecting high-quality data from individual egg cells. Experimental efforts for classifying the mechanical properties of cells are in rich abundance and include, among others, laser optical tweezers [14], optical stretchers [15], magnetic bead measurement [16], and atomic force microscopy (AFM) [17, 18]. For oocytes, the thickness of the outer zona pellucida necessitates slight changes in these classical methods, which also introduces theoretical challenges in the modeling approach. Early experiments used micro tactile sensors to perform shallow indentation (5μm) experiments and measure the Young's modulus of the zona pellucida using Hertz contact [19, 6]. Micropipette aspiration is also common [20, 7, 8], but many assumptions must be employed (i.e. modeling the oocyte as a half-space [21]) in order to determine the mechanical parameters. Some studies used theoretical approaches [4, 5], but model calibration relied on simple linear elasticity assumptions or beam and shell formulations that may not be appropriate for soft materials [6]. More recently, viscoelastic characterization of oocytes has been attempted using micropipette indentation [22], beam deflection [9], and indentation [23, 24, 12]. The complexity of modeling these experiments is quickly increasing, however, and has led to difficulty and uncertainty in obtaining the correct mechanical parameters [23, 24].

Many efforts for increasing the reliability of model calibration in bio-characterization problems have been introduced. For instance, digital image correlation [25] has been used to supplement predictions of FEM simulations in 2D and 3D [26, 27], allowing for *in vivo* mechanical profiling of some biological tissues [28, 29]. Neural networks have been previously incorporated into studies to perform mechanotyping of cell aggregates

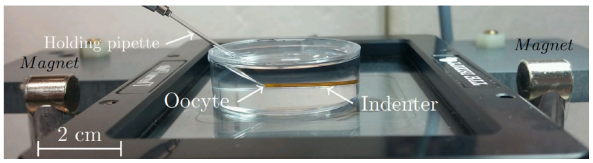

Figure 1: Photograph of the mechanical indentation contraption. The pipette holds an oocyte in front of the indenter inside a Petri dish filled with culture medium (the oocyte diameter is 150 μm and is not visible in the picture).

[30] as well as predict traction profiles within a cell under applied loading [31]. Convolutional neural networks (CNNs) show particular promise in studies that incorporate images [32]. For the oocyte, an inverse FEM method (iFEM) was used to assist in calibrating a mechanical model with three parameters by combining force and image data [23]. Notably, it was found that including image data greatly improved convergence of their optimization strategy. Images have also been used to estimate volume changes of the zona pellucida during indentation [23, 12], where it was speculated that volume change occurs at large deformations due to water expulsion from the porous microstructure. While these studies are promising in their approach, there remains a large variance of mechanical parameters for the oocyte presented in the literature [5, 19, 33, 7]. Without standard metrics for the mechanical properties of the oocyte, it is not possible to select egg cells for ART based on their mechanical response.

In this work, we perform indentation tests on human oocytes in the MII stage of maturation. Indentation is performed with a custom ART-compatible setup using both a flat surface and a sharp indentation tip. To model the oocyte, we use a physically-based mechanical model based on theories of dynamic polymer networks [34, 24]. Ultimately, we propose a novel tool to interpret indentation data using a mechanical model of the experiment and neural networks. We begin by describing our ART-compatible experimental protocol, which gathers force-depth data during indentation. We next describe our mechanical model for the oocyte, which is parameterized by physical quantities. Finally, we calibrate and fit our mechanical data using a neural network that was trained on finite element simulations of the same indentation experiment. The results are separated into two sections: (i) mechanical calibration results of our nine oocytes and (ii) a theoretical methodology for decoupling cell component responses using images and mechanical data.

2. Experiments

For this study, a mechanical characterisation platform has been specially designed to fulfill all the requirements of ART (Fig. 1). This platform (patented under the number WO2018172688: device for mechanically characterising an element of interest such as an oocyte), takes individual human oocytes for classification and is located at the ART center in the Regional University Hospital of Besançon. Each one comes from supernumerary oocytes excluded from the intracytoplasmic sperm injection (ICSI) procedure of patients who have started an ART protocol in Besançon hospital. Please refer to the Appendix for images of each

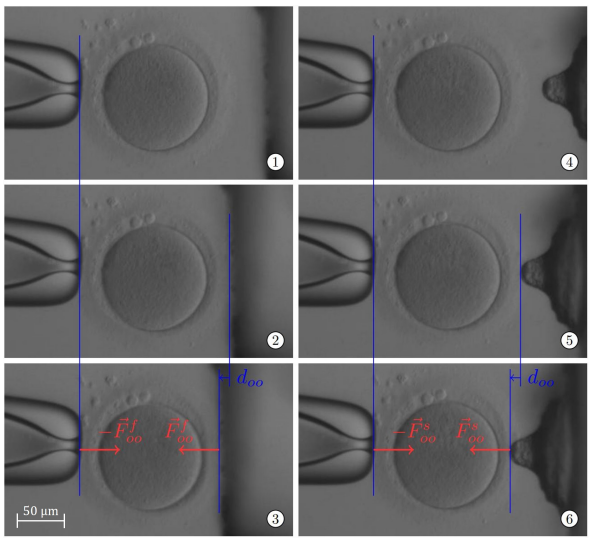

Figure 2: Oocyte indentation test using a flat (left) or a sharp indenter (right). The first photograph (1/4) is taken before beginning the experiment. The second photograph (2/5) is taken the moment the indenter makes contact with the oocyte. The final photograph (3/6) is at the maximum indentation depth of 10μm.

oocyte take before indentation. The following section provides further details of our experimental procedure.

2.1. Oocyte preparation

Each tested oocyte comes from a regular ICSI protocol. First, the cumulus cells surrounding the oocyte are cleared away by association of hyaluronidase digestion for about 20 seconds. Then, a mechanical removal of the cumulus is performed using denudation pipettes. Finally, oocytes are rinsed in IVF medium and individually observed under an inverted microscope (×200 magnification). The mature oocytes at the metaphase II (MII) meiotic maturation stage, with the presence of the first polar body and the absence of germinal vesicle, are reserved for the assisted reproductive technology (ART) and not characterized here. The remaining immature oocytes are incubated in the usual IVF medium at 37°C and 5% CO2 for a duration of 1 to 3 hours. It should be noted that in these culture conditions, some oocytes can progress to the final maturation process and reach the MII stage. The use of these immature oocytes has been approved for our experiments by the clinical ethics committee of The Besancon University Hospital on June 9th 2010. We finally note that approval by the ethics committee is still going on, preventing us to test oocytes that will be transferred to patients.

2.2. Experimental platform

After cumulus removal and rinsing, the oocytes are tested on a patented indentation platform using both flat and sharp indenters. This platform is a modified intracytoplasmic sperm injection (ICSI) platform that includes a nanoforce sensor based on a linear magnetic spring with a typical stiffness of 0.001 N/m [35]. A

magnetic device is used to generate the indentation trajectory – note that the magnetic field is quasi-static and of very low amplitude, thus having no noticeable effects on the cells. More details on this may be found in Gana et al [36]. This platform is used to characterize oocytes by working in a standard Petri dish filled with culture medium and by adding a magnetic indenter. The indenter, an 0.85 mm diameter glass tube of 14 mm length and 5.6 mg weight, applies a controlled compression onto the egg. Indenter position is measured by both external magnetic and electromagnetic devices (see the two magnets on Fig. 1). Once an oocyte is placed in front of the indenter tip, an advanced position feedback control system [37, 38] ensures the user-defined indentation trajectory. The force measurement is performed with the use of an extended-state Kalman filter (ES-LKF) that dynamically estimates the force F_{oo} applied by the indenter tip on the oocyte [39] as it is displaced to the user-controlled distance, $d_{oo}(t)$ (Fig. 2).

Tests were performed using a flat surface or with a sharp shape, which is effectively a sphere of radius 5 μm (see Fig. 2). The recovered data are indentation force, displacement curves versus time and optical images at different stages of loading. There are six image references corresponding respectively to the initial state before loading (1/4), the indenter contact state at zero force (2/5), and the maximum displacement state (3/6) for both flat or sharp indenter shape (See labels in Fig. 2). The stress relaxation response of a set of nine different oocytes was obtained using this procedure. An indentation depth of $\delta = 10\mu$m was applied at a rate of $\dot{\delta} = 1\mu$m/s. The indentation was then held fixed for 50 seconds to allow for relaxation.

3. Physical model of the human oocyte

Each oocyte consists of five primary structures as depicted in Fig. 3. In mature oocytes (MII stage), there is also a polar body inside the perivitelline space. The second polar body is only extruded after fertilization and is not taken into account in this study. While the morphological structure of the perivitelline space and the polar body have been linked to fertility success [40], little is known regarding their mechanical properties. Furthermore, the perivitelline space is largely nonuniform and its exact structure varies between oocytes. To incorporate these into an indentation study would, thus, require a detailed morphological characterization of each oocyte, which is outside the scope of this study. Finally, the oolemma is a $\approx$ 5nm plasma membrane of lipids and proteins surrounding the cytoplasm [41, 42]. While the damage behavior of this structure has been linked to fertility [43, 44, 45], its stiffness is not large enough to contribute to the global mechanical response at small indentations (less than $\approx 20\mu$m) [46, 47, 48].

We therefore devote our primary attention to the cytoplasm and the zona pellucida. We note that for our indentation tests, the contact zone is largely homogeneous [49], and the Saint-Venant heterogeneity effect may be neglected in the cytoplasm. As both the zona pellucida and the cytoplasm are comprised of networks of filaments and proteins, we begin by outlining a general formulation for the mechanics of dynamic polymer networks. The general theory is then specialized for the cases of these components.

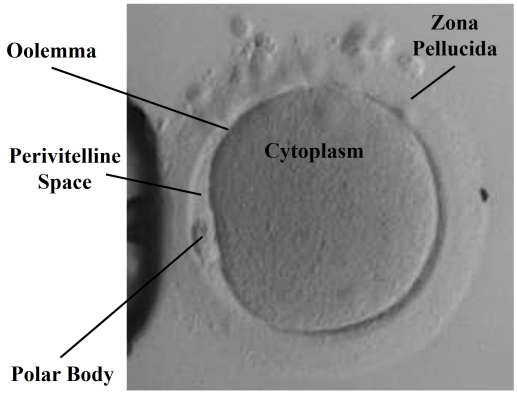

Figure 3: Photograph of an oocyte being held by a micropipette. The primary components of the human oocyte in the MII stage are labeled for convenience.

3.1. Kinematic description of polymer networks

The theory begins with a statistical description of the bio-polymer network, based on the end-to-end vector $\boldsymbol{r}$ of chains, which exist between two crosslinking junctions [34, 50]. In biopolymers, these chains have diverse structures that may be rigid, semi-stiff, or flexible [51]. In turn, their interactions may be unchanging with time (static), dynamic, or a combination of the two (Fig. 4). Within a full network, there exists a distribution $P(\boldsymbol{r})$, which describes the likelihood of a particular chain having end-to-end vector $\boldsymbol{r}$. In this case, the alignment and state of stretch of the network is described at the macro-scale by the conformation tensor $\boldsymbol{\mu} = 3\langle \boldsymbol{r} \otimes \boldsymbol{r} \rangle / r_0^2$, where $\langle \cdot \rangle$ is the statistical averaging operator such that $\langle \cdot \rangle = \int P \langle \cdot \rangle d\boldsymbol{r}$. This tensor thus embeds a description of the current average stretch of a chain in the network and is similar to an Eulerian elastic strain measure. When the network is stress-free, the spherical identity tensor is retrieved (i.e., $\boldsymbol{\mu}_0 = \boldsymbol{I}$), indicating that there is no elastic strain in the network.

We consider the polymer network to exist within each point of a continuum body $\Omega_0 \in \mathbb{R}^3$. When deformed, the motion $\boldsymbol{\chi}(\boldsymbol{X}, t)$ describes how each point $\boldsymbol{X} \in \Omega_0$ moves to its current position $\boldsymbol{x} \in \Omega$. We define the deformation gradient $\boldsymbol{F} = \partial \boldsymbol{\chi} / \partial \boldsymbol{X}$ to describe the mapping for a line element $d\boldsymbol{X} \in \Omega_0$ to its deformed state $d\boldsymbol{x} \in \Omega$. If the chains deform affinely, the instantaneous evolution of an end-to-end vector $\boldsymbol{r}$ is defined by the velocity gradient of the macroscopic body $\boldsymbol{\ell} = \partial \dot{\boldsymbol{x}} / \partial \boldsymbol{x}$ as $\dot{\boldsymbol{r}} = \boldsymbol{\ell} \boldsymbol{r}$ [34].

Let us consider two types of networks, which we will refer to as 'static' and 'dynamic' in nature (Fig. 4). Static networks, which are assumed to be perfectly elastic, are formed by strongly crosslinked chains that do not reneighbor in time. In dynamic networks, the crosslinking junctions are created by weak bonds, which may dissociate and reassociate at appreciable rates. The chains still behave elastically at small timescales, but release their energy upon detaching. Thus, the motion of $\boldsymbol{r}$ may not be affine at long timescales, as the chain might detach during motion. Each of these network types are commonly found in biological materials in varying concentrations [52]. To characterize the dynamic networks, let us assume

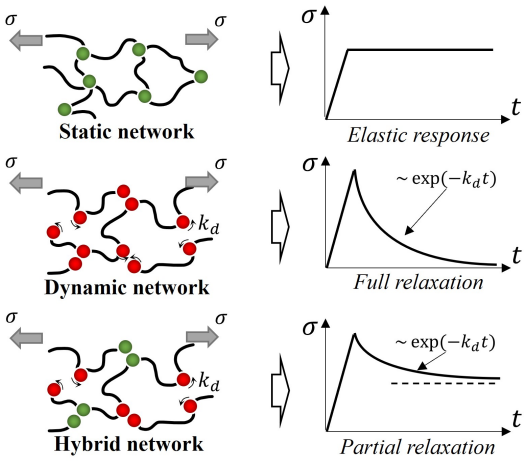

Figure 4: Schematic depiction of static and dynamic polymer networks during a stress relaxation experiment. Static networks deform elastically, while dynamic networks eventually dissipate all energy and relax to zero stress. Hybrid networks exhibit a combination of these behaviors depending on the fraction of static to dynamic bonds.

that chain detachment and reattachment events are defined by a first-order kinetic law and occur with equal probability. We characterize the rate of detachment events by its frequency k_d, measured in units of s^{-1}. We have previously demonstrated [34, 24] the following evolution law for the conformation tensor $\boldsymbol{\mu}$ of the dynamic network:

$$\dot{\boldsymbol{\mu}} = \boldsymbol{\ell}\boldsymbol{\mu} + \boldsymbol{\mu}\boldsymbol{\ell}^T - k_d\left(\boldsymbol{\mu} - \frac{3}{\mathrm{Tr}\,(\boldsymbol{\mu}^{-1})}\boldsymbol{I}\right), \tag{1}$$

where the process of chain kinetics is assumed to behave isochorically, which is enforced by the final term [53]. For the static network, in which the detachment rate k_d is zero, the final term of this equation vanishes. Solving the differential equation in this special case, we observe the conformation tensor of a static polymer network, $\boldsymbol{\mu}_s$, with a net deformation defined by the deformation gradient $\boldsymbol{F}$ to obey the law:

$$\boldsymbol{\mu}_s = \boldsymbol{b} = \boldsymbol{F}\boldsymbol{F}^T. \tag{2}$$

Thus, the conformation tensor of a static network that deforms affinely is equal to the left Cauchy-Green tensor $\boldsymbol{b}$ [34]. Moving forward, the subscript or superscript s denotes a quantity derived for the static network (i.e., $k_d = 0$).

3.2. Energy considerations and constitutive laws

Deforming the macroscopic body stores elastic energy per the local chain stiffness of each constituent network. In the subsequent derivations, we assume an equal-strain treatment that decomposes a multi-component polymer network into the energy stored by chains of the same type (static, dynamic, etc.). The

global deformation $\boldsymbol{F}$ is assumed equal for each network and the stresses $\boldsymbol{\sigma}_i$ of each component are summed for the assembly. For brevity, we omit the subscript i and treat each thermodynamic quantity as describing a single network.

To begin, we assume a form of the free energy density of the network based on dynamic network theory [34]. By summing the energy contributions of each chain in the network, the energy density per unit volume ψ is found to resemble the free-energy density of a Neo-hookean solid [54]. To account for elastic compressibility, we decouple volumetric and isochoric contributions of deformation, yielding the following free energy density:

$$\psi = \frac{ckT}{2}(\operatorname{Tr}\bar{\boldsymbol{\mu}} - 3) + \frac{\kappa}{2}(J_e - 1)^2, \quad J_e = \sqrt{\det \boldsymbol{\mu}}, \tag{3}$$

where c is the density of chains per unit volume, kT is the thermodynamic energy-scale, κ is the bulk modulus of the network, and $\bar{\boldsymbol{\mu}}$ is the isochoric part of the conformation tensor such that $\bar{\boldsymbol{\mu}} = J_e^{-2/3}\boldsymbol{\mu}$. Note that volumetric energy contributions arise only from the elastic parts of volume change defined by J_e. The Cauchy stress $\boldsymbol{\sigma} = 2J_e^{-1}\boldsymbol{\mu}\partial\psi/\partial\boldsymbol{\mu}$ is then derived from this expression to be:

$$\boldsymbol{\sigma} = \frac{ckT}{J_e}\operatorname{dev}\{\bar{\boldsymbol{\mu}}\} + \kappa(J_e - 1). \tag{4}$$

For the static network, $\bar{\boldsymbol{\mu}}$ is replaced by $\bar{\boldsymbol{b}}$ in the above expression and we recover the constitutive law for an incompressible Neohookean solid. Thus, we obtain two simple constitutive laws that can be used to describe static or dynamic components of the oocyte. Given an applied deformation (as defined by the velocity gradient $\boldsymbol{\ell}$), the kinematic equation (1) can be used to solve for the conformation tensor as a function of time, whose solution simplifies to the left Cauchy-Green tensor in the case of a static network. In the following section, we propose a simple modeling strategy for the full oocyte using these two network descriptions.

3.3. Model specialization to each component of the oocyte

The following paragraphs outline a brief physical description of each component of the oocyte along with its approximated network description. The result is a set of six parameters (Table 1) that need to be fit for each oocyte. The parameters are categorized by three physical properties: (i) the density c of static or dynamic chains per unit volume, (ii) the detachment rate k_d of dynamic chains, and (iii) the compressibility κ of the network. Note that the detachment rate defines the relaxation time $\tau = 1/k_d$ of the material.

The cytoplasm. The cytoplasm consists of a viscous fluid and houses various organelles that regulate the functions of the cell. While few studies directly measure the properties of the cytoplasm itself [55], it is generally considered to behave as a viscous fluid. It is known that the organelles rearrange at different stages of maturation, but at the MII stage of our oocytes, an ultrastructural study revealed the distribution

Table 1: Model parameters

Component	Parameter	Units
Zona Pellucida	c_z^s	m^{-3}
	c_z^d	m^{-3}
	κ	Pa
	k_z	s^{-1}
Cytoplasm	c_c	m^{-3}
	k_c	s^{-1}

of organelles to be relatively homogeneous [56]. Further, image analysis of indentation tests has supported the view of the cytoplasm as incompressible [23]. From this, we choose to model the cytoplasm as an incompressible dynamic network, which behaves as a Maxwell element in practice [34, 24]. There is thus one kinematic quantity to track, $\boldsymbol{\mu}_c$, which is the conformation tensor of the cytoplasm. The kinematic equation and constitutive law for this component are then:

$$\dot{\boldsymbol{\mu}}_c = \boldsymbol{\ell}\boldsymbol{\mu}_c + \boldsymbol{\mu}_c\boldsymbol{\ell}^T - k_c\left(\boldsymbol{\mu}_c - \frac{3}{\mathrm{Tr}\,(\boldsymbol{\mu}_c^{-1})}\boldsymbol{I}\right), \qquad \boldsymbol{\sigma}_c = \frac{c_c kT}{J_c}(\boldsymbol{\mu}_c - \boldsymbol{I}) + p(J_c - 1). \tag{5}$$

Here, c_c is the number density of effective chains per unit volume and k_c is the characteristic rate of detachment. These parameters ultimately govern the effective stiffness of the cytoplasm and it relaxation time, respectively. The pressure p acts as a Lagrange multiplier to constrain the incompressibility condition.

The zona pellucida. The zona pellucida is perhaps the most complex structure found in the oocyte. This, combined with the compiling evidence of the importance of its mechanical properties, provides sufficient motivation for using a physically based model to predict its mechanical response. The underlying structure consists of four glycoproteins meshed in tight bundles [49]. Some of these filaments are responsible for binding of sperm and its crossing through the zona pellucida, while others are likely primarily used as structural scaffolding [57, 58]. The latter of which deform with the global deformation, and show little to no reconfiguration. Similar to our previous work [24], we therefore model the zona pellucida as a hybrid network material consisting of one static network and one dynamic network. In this case, there are two conformation tensors to track: (i) the conformation of static chains in the zona, $\boldsymbol{\mu}_z^s$, and (ii) the conformation of dynamic chains in the zona, $\boldsymbol{\mu}_z^d$. The total stress on the assembly is then summed for each network, yielding the following governing equations:

$$\begin{aligned} &\dot{\boldsymbol{\mu}}_z^s = \boldsymbol{\ell}\boldsymbol{\mu}_z^s + \boldsymbol{\mu}_z^s\boldsymbol{\ell}^T, \qquad \dot{\boldsymbol{\mu}}_z^d = \boldsymbol{\ell}\boldsymbol{\mu}_z^d + \boldsymbol{\mu}_z^d\boldsymbol{\ell}^T - k_z^d\left(\boldsymbol{\mu}_z^d - \frac{3}{\mathrm{Tr}\,((\boldsymbol{\mu}_z^d)^{-1})}\boldsymbol{I}\right), \\ &\boldsymbol{\sigma}_z = \frac{c_z^s kT}{J_z^s}\mathrm{dev}\{\bar{\boldsymbol{\mu}}_z^s\} + \frac{c_z^d kT}{J_z^d}\mathrm{dev}\{\bar{\boldsymbol{\mu}}_z^d\} + \kappa(J_e - 1). \end{aligned} \tag{6}$$

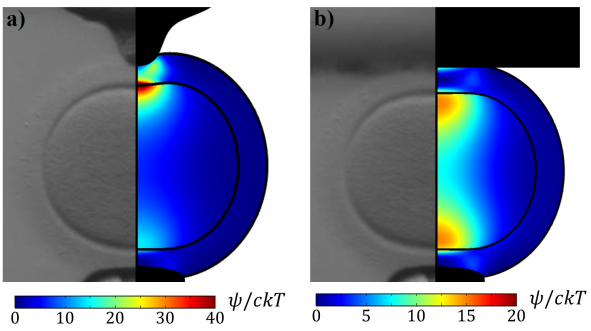

Figure 5: Comparison of FEM simulations with experimental images for sharp (a) and flat indentation (b). The elastic energy, ψ, is normalized by the chain density c of the respective component (zona pellucida or cytoplasm).

Here, the number density of static chains per unit volume is denoted c_z^s, while that of the dynamic chains is c_z^d. The dynamic chains detach at a constant rate k_z, and the volumetric deformation of the network is described by its combined effective bulk modulus κ. Note that, in practice, the solution given in Eq. (2) is used for the conformation tensor of the static network instead of propagating its value in time. We also note that the zona pellucida has been show to exhibit high poroelastic behavior when compressed [12]. In this work, however, they illustrate that significant volumetric changes (and, in turn, poroelastic behavior) are not present for small indentation depths (as defined by the ratio of the indentation depth δ to oocyte radius R approaching zero). All of the experiments that we perform meet this criteria, thus, we neglect the poroelastic response in the current work.

4. Methodology: Finite Element Simulations and Neural Networks

The model presented in the previous section outlines six independent parameters to fit for each indentation experiment. Due to this and the complexity of the oocyte, performing this fitting Would be costly and challenging for a typical optimization strategy (e.g., Nelder-Mead or genetic algorithm). Instead, we take advantage of a simple regressive neural network to solve the inverse problem using a global set of training data that can be quickly obtained by running Finite Element problems in parallel. This section provides an overview of the simulations, neural network definitions, and calibration methodology.

4.1. Finite Element simulations

All simulations are performed in the commercial software COMSOL Multiphysics® using the Structural Mechanics Module. To simplify the geometry and provide a clearer comparison to our images, the oocytes were approximated an axisymmetric body that is initially a sphere. For each oocyte, we used image analysis to determine the correct approximate radius of the body as well as the thickness of the zona pellucida. This was done by collecting data points on both the membrane and the outer zona pellucida using a Canny

algorithm and then fitting them each to a circle using a least-squares approximation. Note that these steps were performed on images of free oocytes (before being in contact with the indenter). The contact problem was solved using a lagrange multiplier method for highest accuracy. To model each compartment, the reduced Transient Network Theory [34] (described in the previous section) was programmed into the external materials interface using a dynamically-linked library. A numerical approximation [59] was used for the material consistent tangent to maintain the Eulerian description of the Transient Network Theory in a Lagrangian context.

The outputs of the FEM simulations are: (i) the total (summed) contact force on the indenter during the simulation and (ii) the displacement profiles of each compartment. Figure 5 illustrates a comparison of the FEM simulations immediately following the loading phase for both sharp and flat indentation. While we have not yet incorporated the deformation profiles of the cytoplasm and zona pellucida into our fitting, a good agreement can be observed between the FEM simulations and experiments. For flat indentation, the elastic energy is much higher, but more localized to the region surrounding the indenter tip. The profiles of the oocyte, including that of the cytoplasm, are found to match well with the images taken at maximum loading.

4.2. Neural network definition and calibration

We formally define the inputs of our neural network as the solution set $\boldsymbol{Y} := \boldsymbol{f} \in \mathbb{R}$, where $\boldsymbol{f}$ is the force history during loading. With the set of material parameters $\boldsymbol{X} := \{c_z^s, c_z^d, \kappa, k_z, c_c, k_c\}$, the mechanical model presented in the previous section defines the forward map $\Phi : \boldsymbol{X} \rightarrow \boldsymbol{Y}$. The objective of our neural network is to determine the inverse map $\Phi^{-1} : \boldsymbol{Y} \rightarrow \boldsymbol{X}$. A reasonable range of material parameters was obtained by determining the largest and smallest cited values of shear moduli and relaxation times reported in the literature [7, 60, 12, 24]. We then applied a generous buffer of 1.5 times this range to define the set of material parameters $\boldsymbol{X} := \{c_z^s, c_z^d, \kappa, k_z, c_c, k_c\}$ to train our neural network. We sampled this set using a stratified sampling technique to obtain 1500 unique simulations that uniformly span the set $\boldsymbol{X}$. Finally, each material parameter was normalized between 0 and 1 before training to improve convergence.

In this study, one advantage of using neural networks is for their convenience in reusing the same simulations as training data. By running our simulations on high performance computing clusters, collecting 1500 unique simulations was much faster than attempting to fit data using any simple optimization scheme that relies on running new simulations during optimization (thus being difficult to run in parallel). The architecture of our neural networks was kept as simple as possible to avoid overfitting the data. For networks only calibrating force data, the first layer (following input) performed convolution to normalize the size of the dataset to exactly 75 points (this number was chosen by observation to work well with our particular problem). Following normalization and ReLU activation (standard after convolutional layers [61]), the next layers of the network consisted of four fully connected layers of size 75, 75, 25, and 6, respectively. Finally, a

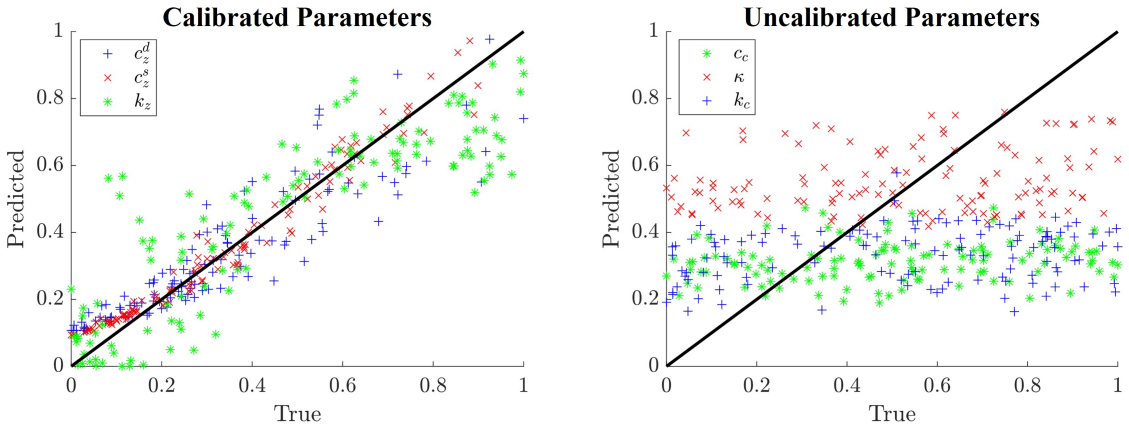

Figure 6: Training verification on a representative set of simulations after neural network calibration at $\delta = 10\mu$m. (left) Parameters that the network was able to predict accurately after training. (right) Parameters that the network was not able to predict accurately after training. All parameters normalized between 0 and 1 for visualization.

sigmoidal activation layer was used before regression to constrain output to our defined range. The regressive neural networks were then trained using Adaptive Moment Estimation (Adam) over 10 epochs on 85% of the training data, with 15% being reserved for validation.

Fig. 6 illustrates a summary of the trained network's predictions versus the true value of our reserved training data. Deviations from the straight line indicate errors in the prediction of the neural network; if accuracy were 100%, all data points would lie on the black line. We find that the network is not able to accurately predict all six of the material parameters listed in Table 1. For the calibrated parameters, we may quantify the degree of agreement with the coefficient of determination R^2, whose value is $R^2 = 0.76$, $R^2 = 0.82$, and $R^2 = 0.92$ for k_z, c_z^d, and c_z^s, respectively. While this does not demonstrate excellent fitting, it is sufficient for performing a fitting as will be demonstrated in the next section. Furthermore, our findings indicate that the force response at this level of indentation is insensitive to the properties of the cytoplasm, within a reasonable range. Thus, the network is inclined to 'guess' for these parameters, resulting in a horizontal bias at values around the mean of its trained data near 0.5 (Fig. 6b). For these parameters, the R^2 is negative, indicating that the mean value of the dataset is a better fit than the black line in the figure. The next section provides an analysis of the material parameters that were calibrated successfully.

5. Results: Mechanical calibration

The verification data presented in Fig. 6 indicates that the network was not able to learn the properties of the cytoplasm and the compressibility of the zona pellucida. Thus, the map $\Phi^{-1} : \boldsymbol{Y} \to \boldsymbol{X}$ is nonconvex for the full set of material parameters. One possible explanation for this is that at small indentations depths, these material parameters do not contribute significantly to the response. As sharp indentation yields a more

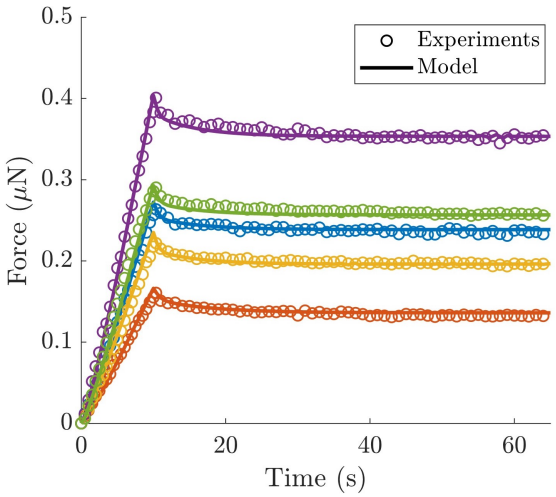

Figure 7: Model comparison to fitted experimental datasets for five of nine oocytes. All calibrated curves were within 5% relative error of the model (including those not illustrated for clarity).

localized response, we focus our material calibration on experiments done with the flat indenter.

5.1. Small-strain flat indentation: properties of the zona pellucida

The neural network successfully output estimates for the properties of the zona pellucida for all nine of our oocytes. Table 2 provides ranges for the shear modulus of the static network, the shear modulus of the dynamic network, and the relaxation time of the zona pellucida (chosen to match more closely with the notation of linear viscoelastic models). After minor manual calibration, we ran FEM simulations with the corresponding material parameters. The resulting force vs. time curves are illustrated in Fig. 7 for five of the nine oocytes (reduced for brevity and illustration - note that the relative error for all fits was within 5%). We observed an excellent fitting for the model and experiments for all experiments.

Table 2: Fitted material properties of the zona pellucida

Property	Definition	Range	Units
Static modulus	$c_z^s kT$	1.3 ± 0.05	kPa
Dynamic modulus	$c_z^d kT$	0.51 ± 0.11	kPa
Relaxation time	$1/k_z$	8.9 ± 0.11	s

Note that the equivalent instantaneous shear modulus of our model is the sum of the static and dynamic modulus, around 2.8 kPa (which assumes a sufficiently quick loading rate). The shear modulus of the zona pellucida in oocytes is typically reported in the literature to be on the order of 1 kPa [5, 19, 33, 7], but its value may depend on the experiment and theoretical model used as well as the species of oocyte. For human oocytes, there have been reported values of $1.0 - 1.5$ kPa using microinjection [62] and $2.0 - 2.5$ kPa

using micropipette aspiration [7]. This is in good agreement with our results, as the combined static and dynamic moduli should reflect a limiting maximum shear modulus. Our results indicate that the structural static network more heavily influences the response due to the higher concentration of static chains. The magnitude of the relaxation behavior is controlled by the relative size of the dynamic network, which relaxes approximately 15% of the stress placed on the oocyte during loading before reaching an equilibrium.

The viscoelastic properties of the oocyte are much less frequently reported in the literature. Further, most studies reporting time-dependent properties are tested on murine or porcine oocytes, which can vary greatly in size and mechanical properties than human oocytes. For instance, one study that used micropipette indentation on murine oocytes reported relaxation times of $2.3-4.0$ s [22]. Another study used micropipette aspiration and reported two relaxation times of 1.7 s and 14 s, respectively [63]. To our knowledge, there has not yet been a study reporting on the relaxation time of human oocytes. Our results indicate that the relaxation time of the human zona pellucida is on the order of 10 seconds. Note that the relaxation curves in Fig. 10 are well-approximated by a single relaxation time. This indicates that, in these experiments, relaxation was dominated by a single timescale – that of the dynamic network in the zona pellucida.

5.2. Sharp indentation: local response reveals softening of the zona pellucida

In a previous study [24], our group hypothesized that indentation using a sharp object would directly probe the properties of the zona pellucida, allowing us to decouple its response from the cytoplasm and that of the global body. To check this hypothesis, we performed indentation using a sharp indenter following the initial round of experiments. These new data form the superset $\boldsymbol{Y}^2 := \{\boldsymbol{f}_f, \boldsymbol{f}_s\}$, where $\boldsymbol{f}_f$ is the flat indentation force vector and f_s is the sharp indentation vector. We then train a neural network to determine the map $\Phi^{-1} : \boldsymbol{Y}^2 \rightarrow \boldsymbol{X}$ using the same parametric space as in the previous section.

After training, we determined a new set of material parameters for each oocyte. Notably, the addition of sharp indentation data did not change the predictions of the network by a significant margin. We ran FEM simulations with the calibrated material parameters to compare the predicted response of the model. In this case, the model consistently overestimated the behavior of the sharp indenter (Fig. 8). Two clear deviations from the model are noted: (i) the slope of the experimental loading curve softens and (ii) the measured amount of stress relaxation is much less than predicted by the model. These two trends were consistently observed for our set of nine oocytes.

The behavior revealed by the sharp indentation experiments implies that our simple model of linear viscoelastic components is not enough to capture the behavior of the oocyte under localized compression. In particular, these trends indicate that much more energy is being dissipated during loading for the sharp indenter. This could be explained by any mechanism that would tend to cause localized softening behavior, which could be an important parameter for characterizing oocytes for their fertilization potential. Due to the fact that less fractional stress relaxation occured, we believe that a reasonable explanation could be

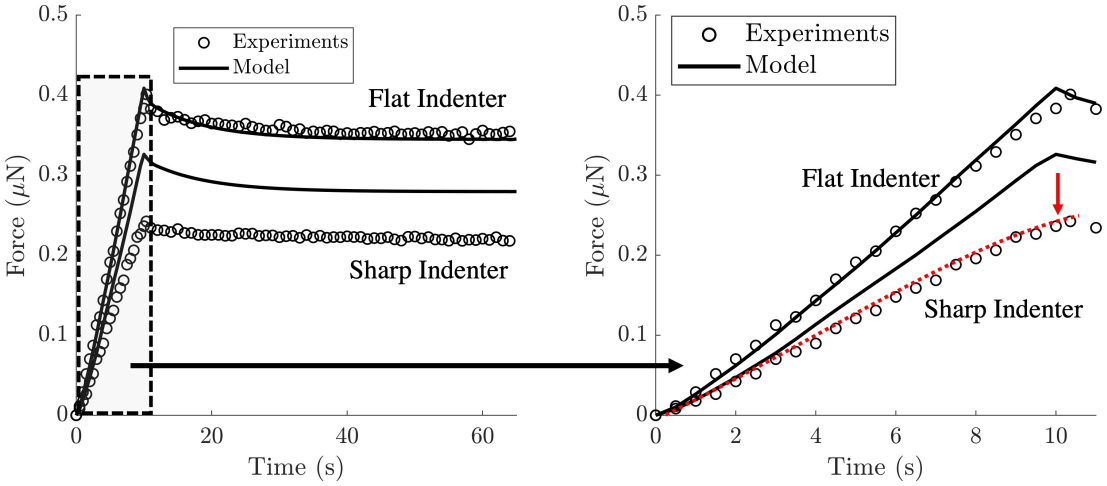

Figure 8: Example of flat and sharp response of one of the nine oocytes. The model overestimates the stiffness of the sharp indentation due to softening of the zona pellucida. The dashed red line is strictly for visualization.

force-accelerated bond kinetics [64]; if the detachment rate of the localized region surrounding the sharp indentation were sensitive to stress, then more relaxation would be induced during loading. Another explanation could be the poroelasticity of the zona pellucida [12]. In one study, the timescale of poroelasticity was cited as roughly three orders of magnitude faster than that of the relaxation in the zona pellucida [65]. While our shallow indentations likely did not induce great volume changes, this mechanism could have influenced our observed force response.

6. Results: Combining images and mechanical data

The approach of creating training data with FEM simulations offers the advantage of running *in silico* experiments to determine experimental protocols that could yield more accurate fitting results. Given the availability of optical images during mechanical tests, we postulate that the cell's deformation profile could provide an important data set to be used for a better parameter estimation. To illustrate the application of including contour data in the calibration procedure, we first present two study cases of simpler systems.

6.1. Elastic indentation of a compressible body

We first consider a single spherical body of radius R that is comprised of a compressible, static network. In this case, the body behaves as a Neohookean material with shear modulus $G = ckT$. The body is indented by a rigid sphere of radius $r = R/2$ up to an indentation depth $\delta = R$. During indentation, we measure the contact force using an augmented Lagrangian method (direct contact method).

Figure 9a illustrates the force-indentation curves and indentation profile of two different bodies. In the first case (blue), we indent a highly compressible body with shear modulus $G = 1.0$kPa. In the second case,

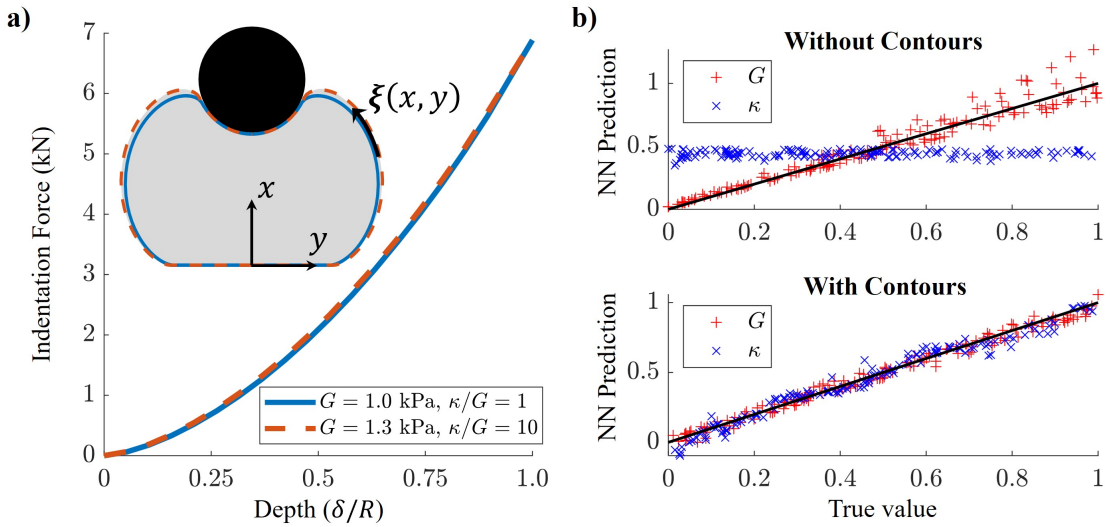

Figure 9: a) Elastic indentation of two compressible bodies with different mechanical properties. For each case, the global (force) response looks nearly identical. b) Performance comparison of network (NN) without and with image contour input. Parameters are normalized between 0 and 1 for visualization.

we indent a nearly incompressible body with shear modulus $G = 1.3$kPa. Even though the compressibility of the two bodies is drastically different, the force-indentation responses look nearly identical. Thus, a typical nonlinear regression fitting procedure would fail to uniquely determine these material parameters, given only the force-displacement curve.

To illustrate this point, we built and trained two neural networks to identify the shear and bulk moduli of the body. To ensure a generalized solution, the domain of shear and bulk moduli, $\mathcal{G}$ and $\mathcal{K}$, respectively, are spanned over four orders of magnitude. We thus seek the inverse map $\Phi^{-1} : \boldsymbol{Y} \rightarrow \boldsymbol{X}$, with $\boldsymbol{X} := \{G, \kappa\} \in \mathcal{G} \times \mathcal{K}$. In the first network, the only input is the force-displacement vector $\boldsymbol{f}$, which defines the solution space $\boldsymbol{Y}_1 := \{\boldsymbol{f}\}$. In the second network, we have included the parameterized curve $\boldsymbol{\xi}$ to define $\boldsymbol{Y}_2 := \{\boldsymbol{f}, \boldsymbol{\xi}\}$. Both networks were trained an the same set of 850 simulations, resulting in two networks.

After training, we sought to verify the convergence of our networks and investigate the generality of their predictions. A reserved dataset $\boldsymbol{Y}_r$ with associated material parameters $\boldsymbol{X}_r$ is was run through each trained network to check their predictions. Figure 9b displays the predicted versus true values for verification. Clearly, the network without contour input is unable to identify the correct bulk modulus using only the force-displacement information. For this reason, it tends to output 0.5, or half of the average value it was trained on. In contrast, the network with image input was able to identify the shear modulus and bulk modulus for each case even over this large range of parameters.

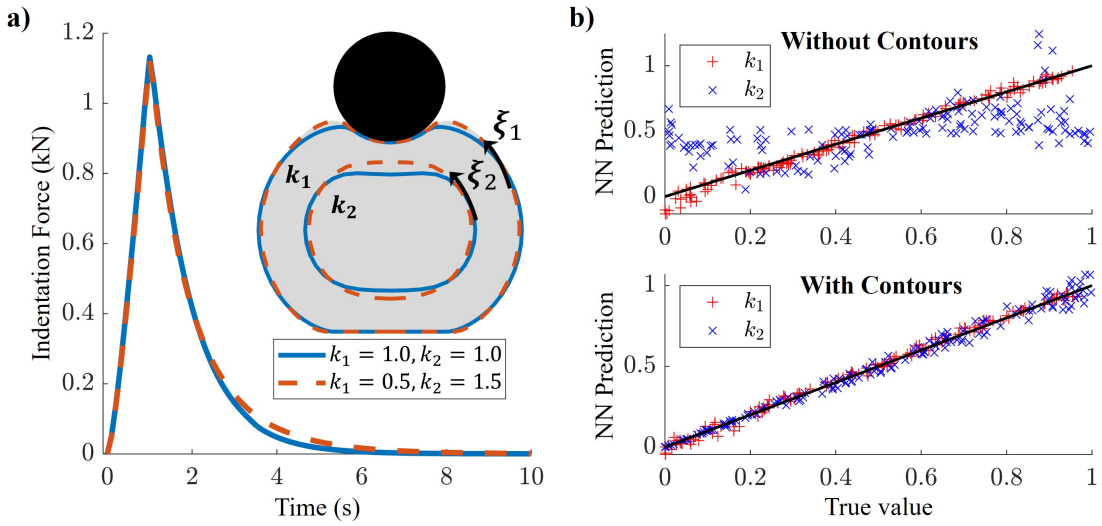

Figure 10: Indentation of a multi-body sphere. a) Force-time curves for bodies with two different properties. Contours and force curves follow the same legend. b) Calibrated neural networks (NNs) without and with image contour inputs. Normalized parameters are displayed for visualization.

6.2. Viscoelastic indentation of a multi-body sphere

We next consider the effect of viscoelasticity on the indentation of a multi-layered body. Here, there is a competition between the deformation of the first layer, which tends to distort the center, and the two distinct timescales defining each layer. This is thus a particularly challenging inverse problem to solve as the elastic and viscoelastic contributions of each compartment are fully coupled to the response of the body. We again consider indenting a sphere of radius R. The sphere is made from two materials: an inner core of radius $r = 0.8R$ and an outer shell. As in the human oocyte, we here consider both materials to be comprised of dynamic networks with different relaxation times. In this case, we maintain an incompressible formulation for simplicity.

To define the solution space $\boldsymbol{X}$, we first note that the elastic stiffness of the body does not change the solution other than scaling the force-indentation curve. As our training data is normalized, we then only need to be concerned with the ratio of shear moduli G_1/G_2, of the outer layer to the inner layer. Upon running multiple sets of training data with varying ratios, we notice no difference in performance of the neural network. We therefore maintain the ratio $G_1/G_2 = 0.5$ for simplicity. As each timescale $k_i, i = 1, 2$ represents the same property, they are defined on the same domain $\mathcal{T}$, which varies four orders of magnitude. The solution space for this problem is thus defined by $\boldsymbol{X} := \{k_1, k_2\} \in \mathcal{T} \times \mathcal{T}$.

As illustrated in Figure 10a, this situation has a very similar non-uniqueness when considering a large range of kinetic rates (relaxation times). In the first test (solid blue curve), the kinetic rates of each network are equal. In the second test (dashed orange curve), the inner core relaxes three times as fast as the outer

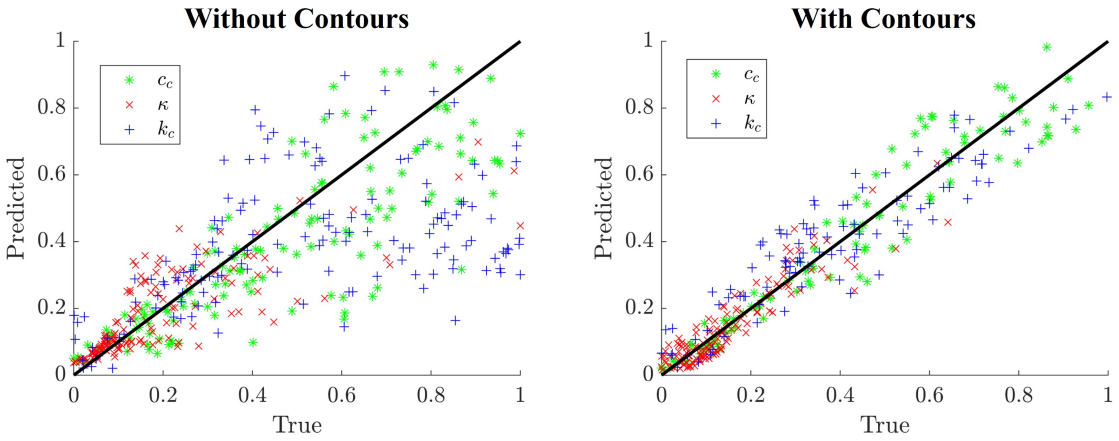

Figure 11: Training verification on a representative set of simulations after neural network calibration for indentation of $\delta = 40\mu$m with and without taking into account contour input. Before introducing contour data, the network is unable to predict the correct material paramters even at a higher indentation.

shell, but the average of their kinetic rates is the same. As a result, the global relaxation response looks nearly identical. The contours of each compartment, however, are drastically different. We thus expect that a regression procedure that incorporates the deformation profiles of the body would perform better.

To this hypothesis, we again train two neural networks on an identical set of 850 training simulations. The solution space for the first network $\boldsymbol{Y}_1 := \{\boldsymbol{f}\}$ remains the same, but the second network now includes two parameterized curves to form $\boldsymbol{Y}_2 := \{\boldsymbol{f}, \boldsymbol{\xi}_1, \boldsymbol{\xi}_2\}$. After training, we perform the same verification procedure as in the previous section. Fig. 10b then displays the predictions of our networks versus their true values. Once again, the network that incorporated image inputs performed significantly better at decoupling the difference in relaxation times between the two components.

6.3. Large-strain oocyte indentation: influence of contours

The minimally invasive restrictions on testing oocytes for ARTs inhibits performing large indentation studies on our oocytes. However, for the 10μm indentations that we performed, we found that the contours of the oocyte do not vary significantly enough to provide any data into our fitting procedure. We therefore offer an *in silico* experiment to illustrate the benefits of including contour data in the large-strain indentation of oocytes. To do this, we created a new set of training data at an indentation of $\delta = 40\mu$m using our FEM model. As before, the FEM model output force vs. time curves as well as contour data for both flat and sharp indenters. The network was trained on the same set of parameters as in the previous section, and the architecture was maintained by only scaling the size of the fully connected layers.

After training the network, we performed a verification test using 15% of the total data set (this data had not been used to train the network). The verification data is presented in Fig. 11 after training the

neural network on only force-time data (left) and on including contour data (right). In both plots, we see a noticeable improvement from the data in Fig. 6. Clearly, at larger indentations, the cytoplasm has a much more significant contribution to the mechanical response of the oocyte.

The contribution of including contour data into the training data is clearly illustrated in Fig. 11. Although the network is able to capture the general trends with only force-time data, its accuracy is low. The network trained with contour data displays greatly improved accuracy. Thus, we conclude that the deformation patterns of the oocyte are largely a function of the compressibility of the zona pellucida and the properties of the cytoplasm.

7. Conclusion

Properly characterizing the mechanical properties of human oocytes could provide an objective way to assess its reproductive potential before use in ART. The end goal of this several year-long project is to be able to select oocytes with the highest chance of successful pregnancy initiation and birth. In order to provide the physician with an effective tool to measure those properties from indentation experiments, we designed an experimental protocol that is fully compatible with ART laboratory standards. To improve our chances of calibrating relevant material parameters, our theoretical modeling approach uses only physical parameters that directly relate to the structure of the oocyte. While this study was only able to confidently predict the properties of the zona pellucida, our procedure indicates two key findings: (i) the zona pellucida exhibits nonlinear material behaviors during localized deformations (i.e., strain or strain-rate dependent softening), and (ii) the deformation profiles of the oocyte are reflective of the properties of the cytoplasm and the compressibility of the zona pellucida.

The softening of the zona pellucida could be explained by several mechanisms. Our initial findings indicate that the relaxation time behaves nonlinearly with large stress concentrations, which could be explained by a force-dependent kinetic rate law such as Bell's law [66]. This approach was shown previously to result in nonlinear viscoelastic behavior such as shear thinning [64], which would be realized as softening in a relaxation test. Other studies have shown that the zona pellucida exhibits strongly time-dependent poroelastic behavior [12], which could also be considered in our simulations. Due to the small indentation depth of this study, however, we do not believe that poroelasticity is significant. Finally, damage of the underlying dynamic network could be considered [67]. This could be investigated by testing the same oocyte and observing consistent and subsequent softening.

The limitation of using a small indentation depth creates a significant challenge in using all available data for calibrating a mechanical model. Although we have illustrated that contour data is highly valuable in isolating the contributions of the cytoplasm and the zona pellucida, there is not a large enough deviation in the deformation profiles for it to be useful in the experiments performed in our lab. Future work with oocytes

that permit large indentations could, however, be aimed at combining optical images of oocytes to calibrate their mechanical behavior. It is important to note that, in contrast to our FEM simulations, the oocyte is not a perfect sphere. Thus, future experiments that include image data of real oocytes must consider the effect of asymmetry, as well as bias due to the imaging technique. Possible approaches could include taking images of the oocyte from multiple angles as well as post-processing techniques to approximate an axisymmetric slice of the body. These techniques could provide a promising avenue for narrowing the range of possible material properties for the cytoplasm, as there is still much uncertainty of its physical range in the literature.

8. Acknowledgments

FJV gratefully acknowledges the support of the National Science Foundation under Award Nos. 2029699 and 1761918. The content is solely the responsibility of the authors and does not necessarily represent the official views of the National Science Foundation. The experimental development is funded by SATT-Sayens and supported by the EUR EiPHi Graduate school (contract “ANR-17-EURE-0002”).

Appendix

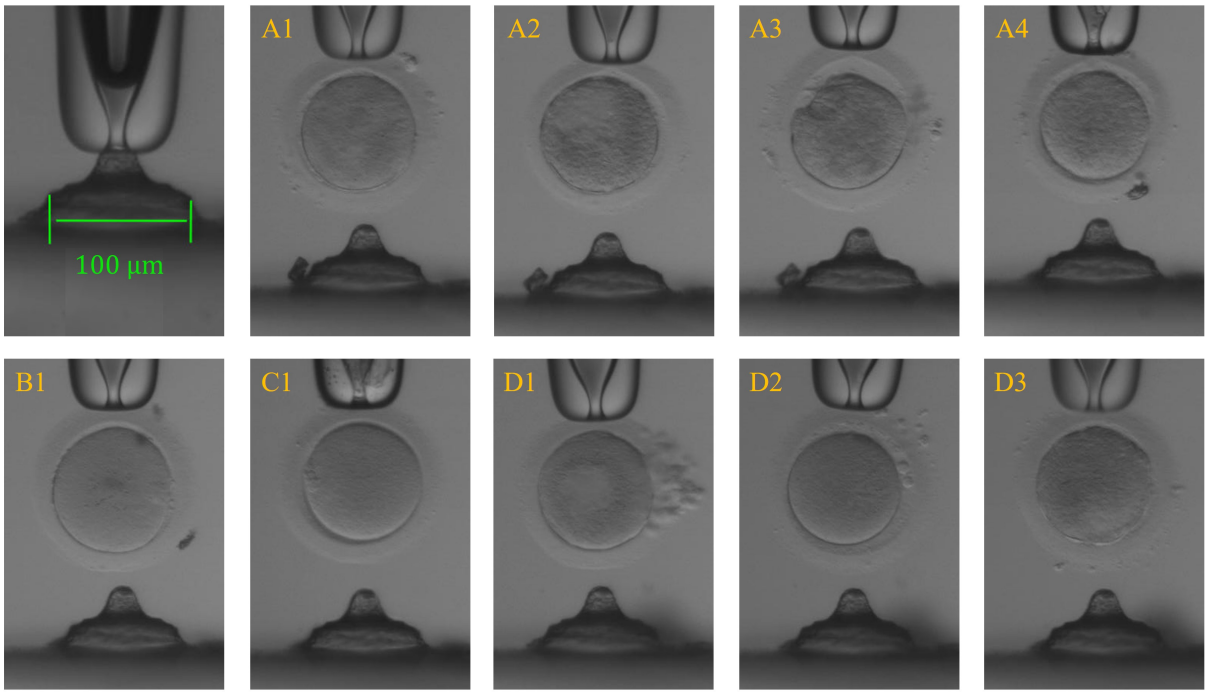

Figure 12: Images of all tested oocytes. Oocytes were taken from four patients who have started an ART protocol. Letters designate the patient of origin.

Figure 13: High resolution images taken of oocytes D1, D2, and D3 for morphological analysis.

References

[1] B. N. Narasimhan, M. S. Ting, T. Kollmetz, M. S. Horrocks, A. E. Chalard, J. Malmström, Mechanical Characterization for Cellular Mechanobiology: Current Trends and Future Prospects, Frontiers in Bioengineering and Biotechnology 8.
URL https://www.frontiersin.org/articles/10.3389/fbioe.2020.595978

[2] W. C. Bae, C. W. Lewis, M. E. Levenston, R. L. Sah, Indentation testing of human articular cartilage: Effects of probe tip geometry and indentation depth on intra-tissue strain, Journal of Biomechanics 39 (6) (2006) 1039–1047. doi:10.1016/j.jbiomech.2005.02.018.
URL https://www.sciencedirect.com/science/article/pii/S0021929005001284

[3] S. Ghosh, V. C. Cuevas, B. Seelbinder, C. P. Neu, Image-Based Elastography of Heterochromatin and Euchromatin Domains in the Deforming Cell Nucleus, Small 17 (5) (2021) 2006109, _eprint: https://onlinelibrary.wiley.com/doi/pdf/10.1002/smll.202006109. doi:10.1002/smll.202006109.
URL https://onlinelibrary.wiley.com/doi/abs/10.1002/smll.202006109

[4] E. Z. Drobnis, J. B. Andrew, D. F. Katz, Biophysical properties of the zona pellucida measured by capillary suction: Is zona hardening a mechanical phenomenon?, Journal of Experimental Zoology 245 (2) (1988) 206–219, _eprint: https://onlinelibrary.wiley.com/doi/pdf/10.1002/jez.1402450210. doi:10.1002/jez.1402450210.
URL https://onlinelibrary.wiley.com/doi/abs/10.1002/jez.1402450210

[5] Y. Sun, K.-T. Wan, K. Roberts, J. Bischof, B. Nelson, Mechanical property characterization of mouse zona pellucida, IEEE Transactions on NanoBioscience 2 (4) (2003) 279–286, conference Name: IEEE Transactions on NanoBioscience. doi:10.1109/TNB.2003.820273.

[6] Y. Murayama, M. Yoshida, J. Mizuno, H. Nakamura, S. Inoue, Y. Watanabe, K. Akaishi, H. Inui, C. E. Constantinou, S. Omata, Elasticity Measurement of Zona Pellucida Using a Micro Tactile Sensor to Evaluate Embryo Quality, Journal of Mammalian Ova Research 25 (1) (2008) 8–16, publisher: Japanese Society of Mammalian Ova Research. doi:10.1274/jmor.25.8.
URL https://bioone.org/journals/journal-of-mammalian-ova-research/volume-25/issue-1/jmor.25.8/Elasticity-Measurement-of-Z

[7] M. Khalilian, M. Navidbakhsh, M. R. Valojerdi, M. Chizari, P. E. Yazdi, Estimating Young's modulus of zona pellucida by micropipette aspiration in combination with theoretical models of ovum, Journal of The Royal Society Interface 7 (45) (2010) 687–694, publisher: Royal Society. doi:10.1098/rsif.2009.0380.
URL https://royalsocietypublishing.org/doi/10.1098/rsif.2009.0380

[8] M. Khalilian, M. Navidbakhsh, M. Rezazadeh Valojerdi, M. Chizari, P. Eftekhari Yazdi, Alteration in the Mechanical Properties of Human Ovum Zona Pellucida Following Fertilization: Experimental and Analytical Studies, Experimental Mechanics 51 (2) (2011) 175–182. doi:10.1007/s11340-010-9357-z.
URL https://doi.org/10.1007/s11340-010-9357-z

[9] J. Kim, J. Kim, Viscoelastic Characterization of Mouse Zona Pellucida, IEEE Transactions on Biomedical Engineering 60 (2) (2013) 569–575, conference Name: IEEE Transactions on Biomedical Engineering. doi:10.1109/TBME.2012.2230444.

[10] L. Z. Yanez, J. Han, B. B. Behr, R. A. R. Pera, D. B. Camarillo, Human oocyte developmental potential is predicted by mechanical properties within hours after fertilization, Nature Communications 7 (1) (2016) 10809, number: 1 Publisher: Nature Publishing Group. doi:10.1038/ncomms10809.
URL https://www.nature.com/articles/ncomms10809

[11] T. Ebner, M. Moser, M. Sommergruber, M. Puchner, R. Wiesinger, G. Tews, Developmental competence of oocytes showing increased cytoplasmic viscosity, Human Reproduction 18 (6) (2003) 1294–1298. doi:10.1093/humrep/deg232.
URL https://doi.org/10.1093/humrep/deg232

[12] A. Stracuzzi, J. Dittmann, M. Böl, A. E. Ehret, Visco- and poroelastic contributions of the zona pellucida to the mechanical response of oocytes, Biomechanics and Modeling in Mechanobiology 20 (2) (2021) 751–765. doi:10.1007/s10237-020-01414-

4.
URL https://doi.org/10.1007/s10237-020-01414-4

[13] L. Rienzi, G. Vajta, F. Ubaldi, Predictive value of oocyte morphology in human IVF: a systematic review of the literature, Human Reproduction Update 17 (1) (2011) 34–45. doi:10.1093/humupd/dmq029.
URL https://doi.org/10.1093/humupd/dmq029

[14] J. Dai, M. Sheetz, Mechanical properties of neuronal growth cone membranes studied by tether formation with laser optical tweezers, Biophysical Journal 68 (3) (1995) 988–996. doi:https://doi.org/10.1016/S0006-3495(95)80274-2.
URL https://www.sciencedirect.com/science/article/pii/S0006349595802742

[15] J. Guck, R. Ananthakrishnan, H. Mahmood, T. J. Moon, C. C. Cunningham, J. Käs, The optical stretcher: A novel laser tool to micromanipulate cells, Biophysical Journal 81 (2) (2001) 767–784. doi:https://doi.org/10.1016/S0006-3495(01)75740-2.
URL https://www.sciencedirect.com/science/article/pii/S0006349501757402

[16] A. R. Bausch, F. Ziemann, A. A. Boulbitch, K. Jacobson, E. Sackmann, Local measurements of viscoelastic parameters of adherent cell surfaces by magnetic bead microrheometry, Biophysical Journal 75 (4) (1998) 2038–2049. doi:https://doi.org/10.1016/S0006-3495(98)77646-5.
URL https://www.sciencedirect.com/science/article/pii/S0006349598776465

[17] J. Schäpe, S. Prauße, M. Radmacher, R. Stick, Influence of lamin a on the mechanical properties of amphibian oocyte nuclei measured by atomic force microscopy, Biophysical Journal 96 (10) (2009) 4319–4325. doi:https://doi.org/10.1016/j.bpj.2009.02.048.
URL https://www.sciencedirect.com/science/article/pii/S0006349509006559

[18] M. Radmacher, Studying the mechanics of cellular processes by atomic force microscopy, in: Cell Mechanics, Vol. 83 of Methods in Cell Biology, Academic Press, 2007, pp. 347–372. doi:https://doi.org/10.1016/S0091-679X(07)83015-9.
URL https://www.sciencedirect.com/science/article/pii/S0091679X07830159

[19] Y. Murayama, J. Mizuno, H. Kamakura, Y. Fueta, H. Nakamura, K. Akaishi, K. Anzai, A. Watanabe, H. Inui, S. Omata, Mouse zona pellucida dynamically changes its elasticity during oocyte maturation, fertilization and early embryo development, Human Cell 19 (4) (2006) 119–125. doi:10.1111/j.1749-0774.2006.00019.x.
URL https://doi.org/10.1111/j.1749-0774.2006.00019.x

[20] R. M. Hochmuth, Micropipette aspiration of living cells, Journal of Biomechanics 33 (1) (2000) 15–22. doi:https://doi.org/10.1016/S0021-9290(99)00175-X.
URL https://www.sciencedirect.com/science/article/pii/S002192909900175X

[21] D. P. Theret, M. J. Levesque, M. Sato, R. M. Nerem, L. T. Wheeler, The Application of a Homogeneous Half-Space Model in the Analysis of Endothelial Cell Micropipette Measurements, Journal of Biomechanical Engineering 110 (3) (1988) 190–199. doi:10.1115/1.3108430.
URL https://doi.org/10.1115/1.3108430

[22] X. Liu, J. Shi, Z. Zong, K.-T. Wan, Y. Sun, Elastic and Viscoelastic Characterization of Mouse Oocytes Using Micropipette Indentation, Annals of Biomedical Engineering 40 (10) (2012) 2122–2130. doi:10.1007/s10439-012-0595-3.
URL https://doi.org/10.1007/s10439-012-0595-3

[23] J. Dittmann, A. Dietzel, M. Böl, Mechanical characterisation of oocytes - The influence of sample geometry on parameter identification, Journal of the Mechanical Behavior of Biomedical Materials 77 (2018) 764–775. doi:10.1016/j.jmbbm.2017.07.037.
URL https://www.sciencedirect.com/science/article/pii/S1751616117303223

[24] T. Shen, E. Benet, S. L. Sridhar, J. Abadie, E. Piat, F. J. Vernerey, Separating the contributions of zona pellucida and cytoplasm in the viscoelastic response of human oocytes, Acta Biomaterialia 85 (2019) 253–262.

doi:10.1016/j.actbio.2018.12.034.
URL https://www.sciencedirect.com/science/article/pii/S1742706118307591

[25] M. Palanca, G. Tozzi, L. Cristofolini, The use of digital image correlation in the biomechanical area: a review, International Biomechanics 3 (1) (2016) 1–21, publisher: Taylor & Francis _eprint: https://doi.org/10.1080/23335432.2015.1117395. doi:10.1080/23335432.2015.1117395.
URL https://doi.org/10.1080/23335432.2015.1117395

[26] B. Ahn, J. Kim, Measurement and characterization of soft tissue behavior with surface deformation and force response under large deformations, Medical Image Analysis 14 (2) (2010) 138–148. doi:10.1016/j.media.2009.10.006.
URL https://www.sciencedirect.com/science/article/pii/S1361841509001224

[27] B. C. Roberts, E. Perilli, K. J. Reynolds, Application of the digital volume correlation technique for the measurement of displacement and strain fields in bone: A literature review, Journal of Biomechanics 47 (5) (2014) 923–934. doi:10.1016/j.jbiomech.2014.01.001.
URL https://www.sciencedirect.com/science/article/pii/S0021929014000037

[28] K. M. Moerman, C. A. Holt, S. L. Evans, C. K. Simms, Digital image correlation and finite element modelling as a method to determine mechanical properties of human soft tissue in vivo, Journal of Biomechanics 42 (8) (2009) 1150–1153. doi:10.1016/j.jbiomech.2009.02.016.
URL https://www.sciencedirect.com/science/article/pii/S0021929009000979

[29] S. L. Evans, C. A. Holt, Measuring the mechanical properties of human skin in vivo using digital image correlation and finite element modelling, The Journal of Strain Analysis for Engineering Design 44 (5) (2009) 337–345, publisher: IMECHE. doi:10.1243/03093247JSA488.
URL https://doi.org/10.1243/03093247JSA488

[30] C. Combs, D. D. Seith, M. J. Bovyn, S. P. Gross, X. Xie, Z. S. Siwy, Deep learning assisted mechanotyping of individual cells through repeated deformations and relaxations in undulating channels, Biomicrofluidics 16 (1) (2022) 014104, publisher: American Institute of Physics. doi:10.1063/5.0077432.
URL https://aip.scitation.org/doi/10.1063/5.0077432

[31] H. Li, D. Matsunaga, T. S. Matsui, H. Aosaki, G. Kinoshita, K. Inoue, A. Doostmohammadi, S. Deguchi, Wrinkle force microscopy: a machine learning based approach to predict cell mechanics from images, Communications Biology 5 (1) (2022) 1–9, number: 1 Publisher: Nature Publishing Group. doi:10.1038/s42003-022-03288-x.
URL https://www.nature.com/articles/s42003-022-03288-x

[32] H. Li, D. Matsunaga, T. S. Matsui, H. Aosaki, S. Deguchi, Image based cellular contractile force evaluation with small-world network inspired CNN: SW-UNet, Biochemical and Biophysical Research Communications 530 (3) (2020) 527–532. doi:10.1016/j.bbrc.2020.04.134.
URL https://www.sciencedirect.com/science/article/pii/S0006291X20308743

[33] E. Priel, T. Priel, I. Szaingurten-Solodkin, T. Wainstock, Y. Perets, A. Zeadna, A. Harlev, E. Lunenfeld, E. Levitas, I. Har-Vardi, Zona pellucida shear modulus, a possible novel non-invasive method to assist in embryo selection during in-vitro fertilization treatment, Scientific Reports 10 (1) (2020) 14066, number: 1 Publisher: Nature Publishing Group. doi:10.1038/s41598-020-70739-y.
URL https://www.nature.com/articles/s41598-020-70739-y

[34] F. J. Vernerey, R. Long, R. Brighenti, A statistically-based continuum theory for polymers with transient networks, Journal of the Mechanics and Physics of Solids 107 (2017) 1–20. doi:10.1016/j.jmps.2017.05.016.
URL https://www.sciencedirect.com/science/article/pii/S0022509617301874

[35] J. Abadie, C. Roux, E. Piat, C. Filiatre, C. Amiot, Experimental measurement of human oocyte mechanical properties on a micro and nanoforce sensing platform based on magnetic springs, Sensors and Actuators B: Chemical 190 (2014)

429–438. doi:https://doi.org/10.1016/j.snb.2013.08.042.
URL https://www.sciencedirect.com/science/article/pii/S0925400513009660

[36] R. Gana, J. Abadie, E. Piat, C. Roux, C. Amiot, C. Pieralli, B. Wacogne, A novel force sensing platform using passive magnetic springs for mechanical characterisation of human oocytes, Sensors and Actuators A: Physical 262 (2017) 114–122. doi:https://doi.org/10.1016/j.sna.2017.01.015.
URL https://www.sciencedirect.com/science/article/pii/S0924424717301000

[37] F. Amokrane, E. Piat, J. Abadie, A. Drouot, J. Escareno, State observation of a specific class of unknown nonlinear siso systems using linear kalman filtering, in: 2019 IEEE 58th Conference on Decision and Control (CDC), 2019, pp. 1595–1600. doi:10.1109/CDC40024.2019.9029614.

[38] F. Amokrane, E. Piat, J. Abadie, A. Drouot, J. Escareno, State observation of unknown nonlinear siso systems based on virtual input estimation, International Journal of Control 0 (0) (2019) 1–14. arXiv:https://doi.org/10.1080/00207179.2019.1680869, doi:10.1080/00207179.2019.1680869.
URL https://doi.org/10.1080/00207179.2019.1680869

[39] E. Piat, J. Abadie, S. Oster, Nanoforce estimation based on kalman filtering and applied to a force sensor using diamagnetic levitation, Sensors and Actuators A: Physical 179 (2012) 223–236. doi:https://doi.org/10.1016/j.sna.2012.02.025.
URL https://www.sciencedirect.com/science/article/pii/S0924424712001288

[40] P. Xia, Intracytoplasmic sperm injection: correlation of oocyte grade based on polar body, perivitelline space and cytoplasmic inclusions with fertilization rate and embryo quality., Human Reproduction 12 (8) (1997) 1750–1755. doi:10.1093/humrep/12.8.1750.
URL https://doi.org/10.1093/humrep/12.8.1750

[41] E. Evans, V. Heinrich, F. Ludwig, W. Rawicz, Dynamic Tension Spectroscopy and Strength of Biomembranes, Biophysical Journal 85 (4) (2003) 2342–2350. doi:10.1016/S0006-3495(03)74658-X.
URL https://www.sciencedirect.com/science/article/pii/S000634950374658X

[42] E. London, Lipid Bilayer Structure, in: W. J. Lennarz, M. D. Lane (Eds.), Encyclopedia of Biological Chemistry (Second Edition), Academic Press, Waltham, 2013, pp. 733–735. doi:10.1016/B978-0-12-378630-2.00114-6.
URL https://www.sciencedirect.com/science/article/pii/B9780123786302001146

[43] Z. Nagy, J. Liu, G. Joris, G. Bocken, B. Desmet, A. van Ranst, A. Vankelecom, P. Devroey, A. van Steirteghem, The influence of the site of sperm deposition and mode of oolemma breakage at intracytoplasmic sperm injection on fertilization and embryo development rates, Human Reproduction 10 (12) (1995) 3171–3177. doi:10.1093/oxfordjournals.humrep.a135881.
URL https://doi.org/10.1093/oxfordjournals.humrep.a135881

[44] G. D. Palermo, M. Alikani, M. Bertoli, L. T. Colombero, F. Moy, J. Cohen, Z. Rosenwaks, Oolemma characteristics in relation to survival and fertilization patterns of oocytes treated by intracytoplasmic sperm injection, Human Reproduction 11 (1) (1996) 172–176. doi:10.1093/oxfordjournals.humrep.a019012.
URL https://doi.org/10.1093/oxfordjournals.humrep.a019012

[45] M. Wilding, L. Di Matteo, S. D'Andretti, N. Montanaro, C. Capobianco, B. Dale, An oocyte score for use in assisted reproduction, Journal of Assisted Reproduction and Genetics 24 (8) (2007) 350–358. doi:10.1007/s10815-007-9143-8.
URL https://doi.org/10.1007/s10815-007-9143-8

[46] F. Campelo, C. Arnarez, S. J. Marrink, M. M. Kozlov, Helfrich model of membrane bending: From Gibbs theory of liquid interfaces to membranes as thick anisotropic elastic layers, Advances in Colloid and Interface Science 208 (2014) 25–33. doi:10.1016/j.cis.2014.01.018.
URL https://www.sciencedirect.com/science/article/pii/S000186861400030X

[47] R. A. Sauer, On the Computational Modeling of Lipid Bilayers Using Thin-Shell Theory, in: D. J. Steigmann (Ed.), The Role of Mechanics in the Study of Lipid Bilayers, CISM International Centre for Mechanical Sciences, Springer

International Publishing, Cham, 2018, pp. 221–286.

[48] J. Dai, M. P. Sheetz, Chapter 9 Cell Membrane Mechanics, in: M. P. Sheetz (Ed.), Methods in Cell Biology, Vol. 55, Academic Press, 1997, pp. 157–171. doi:10.1016/S0091-679X(08)60407-0.
URL https://www.sciencedirect.com/science/article/pii/S0091679X08604070

[49] G. Familiari, M. Relucenti, R. Heyn, G. Micara, S. Correr, Three-dimensional structure of the zona pellucida at ovulation, Microscopy Research and Technique 69 (6) (2006) 415–426, _eprint: https://analyticalsciencejournals.onlinelibrary.wiley.com/doi/pdf/10.1002/jemt.20301. doi:10.1002/jemt.20301.
URL https://analyticalsciencejournals.onlinelibrary.wiley.com/doi/abs/10.1002/jemt.20301

[50] C.-Y. Hui, F. Cui, A. Zehnder, F. J. Vernerey, Physically motivated models of polymer networks with dynamic cross-links: comparative study and future outlook, Proceedings of the Royal Society A: Mathematical, Physical and Engineering Sciences 477 (2255) (2021) 20210608, publisher: Royal Society. doi:10.1098/rspa.2021.0608.
URL https://doi.org/10.1098/rspa.2021.0608

[51] C. Storm, J. J. Pastore, F. C. MacKintosh, T. C. Lubensky, P. A. Janmey, Nonlinear elasticity in biological gels, Nature 435 (7039) (2005) 191–194, number: 7039 Publisher: Nature Publishing Group. doi:10.1038/nature03521.
URL https://www.nature.com/articles/nature03521

[52] S. Lalitha Sridhar, F. J. Vernerey, Mechanics of transiently cross-linked nematic networks, Journal of the Mechanics and Physics of Solids 141 (2020) 104021. doi:10.1016/j.jmps.2020.104021.
URL https://www.sciencedirect.com/science/article/pii/S0022509620302568

[53] T. Shen, F. J. Vernerey, Rate-dependent fracture of transient networks, Journal of the Mechanics and Physics of Solids 143 (2020) 104028. doi:10.1016/j.jmps.2020.104028.
URL https://www.sciencedirect.com/science/article/pii/S0022509620302635

[54] S. Lalitha Sridhar, F. J. Vernerey, The Chain Distribution Tensor: Linking Nonlinear Rheology and Chain Anisotropy in Transient Polymers, Polymers 10 (8) (2018) 848, number: 8 Publisher: Multidisciplinary Digital Publishing Institute. doi:10.3390/polym10080848.
URL https://www.mdpi.com/2073-4360/10/8/848

[55] A. R. Bausch, W. Möller, E. Sackmann, Measurement of Local Viscoelasticity and Forces in Living Cells by Magnetic Tweezers, Biophysical Journal 76 (1) (1999) 573–579. doi:10.1016/S0006-3495(99)77225-5.
URL https://www.sciencedirect.com/science/article/pii/S0006349599772255

[56] Z. Trebichalská, D. Kyjovská, S. Kloudová, P. Otevřel, A. Hampl, Z. Holubcová, Cytoplasmic maturation in human oocytes: an ultrastructural study †, Biology of Reproduction 104 (1) (2021) 106–116. doi:10.1093/biolre/ioaa174.
URL https://doi.org/10.1093/biolre/ioaa174

[57] P. M. Wassarman, Zona Pellucida Glycoproteins, Annual Review of Biochemistry 57 (1) (1988) 415–442, _eprint: https://doi.org/10.1146/annurev.bi.57.070188.002215. doi:10.1146/annurev.bi.57.070188.002215.
URL https://doi.org/10.1146/annurev.bi.57.070188.002215

[58] P. M. Wassarman, C. Liu, E. S. Litscher, Constructing the mammalian egg zona pellucida: some new pieces of an old puzzle, Journal of Cell Science 109 (8) (1996) 2001–2004. doi:10.1242/jcs.109.8.2001.
URL https://doi.org/10.1242/jcs.109.8.2001

[59] C. Miehe, Numerical computation of algorithmic (consistent) tangent moduli in large-strain computational inelasticity, Computer Methods in Applied Mechanics and Engineering 134 (3) (1996) 223–240. doi:10.1016/0045-7825(96)01019-5.
URL https://www.sciencedirect.com/science/article/pii/0045782596010195

[60] L. Andolfi, E. Masiero, E. Giolo, M. Martinelli, S. Luppi, S. dal Zilio, I. Delfino, R. Bortul, M. Zweyer, G. Ricci, M. Lazzarino, Investigating the mechanical properties of zona pellucida of whole human oocytes by atomic force spectroscopy, Integrative Biology 8 (8) (2016) 886–893. doi:10.1039/c6ib00044d.

URL https://doi.org/10.1039/c6ib00044d

[61] I. J. Goodfellow, Y. Bengio, A. Courville, Deep Learning, MIT Press, Cambridge, MA, USA, 2016.

[62] M. Khalilian, M. R. Valojerdi, M. Navidbakhsh, M. Chizari, P. Eftekhari-Yazdi, Estimating zona pellucida hardness under microinjection to assess oocyte/embryo quality: Analytical and experimental studies, Advances in Bioscience and Biotechnology 4 (5) (2013) 679–688, number: 5 Publisher: Scientific Research Publishing. doi:10.4236/abb.2013.45089.
URL http://www.scirp.org/Journal/Paperabs.aspx?paperid=32285

[63] L. Andolfi, S. L. M. Greco, D. Tierno, R. Chignola, M. Martinelli, E. Giolo, S. Luppi, I. Delfino, M. Zanetti, A. Battistella, G. Baldini, G. Ricci, M. Lazzarino, Planar AFM macro-probes to study the biomechanical properties of large cells and 3D cell spheroids, Acta Biomaterialia 94 (2019) 505–513. doi:10.1016/j.actbio.2019.05.072.
URL https://www.sciencedirect.com/science/article/pii/S174270611930399X

[64] S. Lamont, F. J. Vernerey, A Transient Microsphere Model for Nonlinear Viscoelasticity in Dynamic Polymer Networks, Journal of Applied Mechanics 89 (1). doi:10.1115/1.4052375.
URL https://doi.org/10.1115/1.4052375

[65] K. Karimian, R. Seydewitz, D. Töpfer, M. Böl, Poro-viscoelastic behaviour of the zona pellucida: Impact of three-dimensional modelling on material characterisation, Journal of the Mechanical Behavior of Biomedical Materials 131 (2022) 105211. doi:10.1016/j.jmbbm.2022.105211.
URL https://www.sciencedirect.com/science/article/pii/S1751616122001278

[66] G. I. Bell, Models for the specific adhesion of cells to cells, Science 200 (4342) (1978) 618–627, publisher: American Association for the Advancement of Science Section: Articles. doi:10.1126/science.347575.
URL https://science.sciencemag.org/content/200/4342/618

[67] S. C. Lamont, J. Mulderrig, N. Bouklas, F. J. Vernerey, Rate-Dependent Damage Mechanics of Polymer Networks with Reversible Bonds, Macromolecules 54 (23) (2021) 10801–10813, publisher: American Chemical Society. doi:10.1021/acs.macromol.1c01943.
URL https://doi.org/10.1021/acs.macromol.1c01943